Characterization of the Turbulence Structure in Supersonic Boundary Layers using DNS Data

Matthew J. Ringuette[*], M. Pino Martín[†], Alexander J. Smits[‡], and Minwei Wu[§]

Mechanical and Aerospace Engineering Department

Princeton University, Princeton, NJ

A direct numerical simulation database is used to characterize the structure of supersonic turbulent boundary layers at Mach numbers from 3 to 5. We develop tools to calculate the average properties of the coherent structures, namely, angle, convection velocity, and length scale, and show good agreement with the available experimental data. We find that the structure angle and convection velocity increase with Mach number, while the streamwise integral length scale decreases. The structures become taller with Mach number, which is consistent with the larger structure angle. The distribution of the streaky-structure spacing at the wall is computed, and observed to be slightly narrower and more uniform with increasing Mach number. We find that the low-speed streaks carry about one-third of the total turbulent kinetic energy. Similar to the incompressible case, we observe hairpin vortices clustered into streamwise packets at all Mach numbers, and develop an algorithm to identify and characterize these hairpin packets. The average packet convection velocity, length, and number of hairpins increase with higher Mach number, while the packet height and angle decrease.

I. Introduction

Coherent structures in the inner and outer layers of a turbulent boundary layer are thought to play a significant role in the generation of turbulence. Klebanoff[1] found that about 75% of the total production of turbulent kinetic energy takes place in the near-wall region within 20% of the boundary layer thickness. The viscous sublayer has been shown to contain streamwise alternating streaks of low- and high-speed fluid.[2–4] The spanwise spacing of these structures scales on inner variables, having a mean value of about 100 wall units. At incompressible conditions, Smith & Metzler[5] found this spacing to be independent of Reynolds number (Re) for Re_θ = 740 to 5830. For supersonic flow, there are no data on the distribution of the streak spacing and its variation with Mach number. The streaks are formed by extended, counter-rotating streamwise vortices that occur close to the wall. Observations by Kline *et al.*[3] indicate that the streaks slowly lift away from the wall, undulate, and finally break up and eject fluid into the outer region of the boundary layer; this is referred to as a "bursting" event. Experiments by Kim *et al.*[6] indicate that bursting is the primary mechanism of turbulence production within the first 100 wall units away from the wall. The importance of the near-wall region and the bursting process in turbulence production demonstrates the need for a greater understanding of the structure in the inner layer.

[*]AIAA Member
[†]AIAA Member
[‡]AIAA Fellow
[§]AIAA Student Member

Case	M_δ	ρ_δ (kg/m^3)	T_δ (K)	T_w/T_δ	Re_θ	$\theta(mm)$	H	$\delta(mm)$
M3	2.98	0.0907	219.55	2.58	2390	0.430	5.4	6.04
M4	3.98	0.0923	219.69	3.83	3944	0.523	8.5	9.77
M5	4.97	0.0937	220.97	5.40	6225	0.657	12.2	14.82

Table 1. Dimensional boundary-layer-edge and wall parameters for the DNS database.

In the outer layer, beyond the logarithmic region, the flow at moderate Mach numbers is characterized by entrainment through large-scale turbulent "bulges," rather than turbulence production. Also called large scale motion (LSM), the bulges develop and decay slowly, and lean in the downstream direction at acute angles to the wall. Spina *et al.*[7] found that 40% of the outer-layer Reynolds shear stress is generated near the sloping interfaces of the LSM. For supersonic flows, the fundamental properties of the LSM, such as structure angle, length scale, convection velocity, and internal structure, namely, velocity, vorticity, and pressure fields, are the topic of ongoing research.

Previous work[8] has shown evidence that the so-called horseshoe or hairpin vortex is the predominant coherent structure of a turbulent boundary layer. In the horseshoe vortex model, the lifted low-speed streaks act like unstable shear layers and roll up inboard into the transverse vortex, or "head," of the horseshoe, becoming the sides, or "legs," outboard.[9] Complete hairpins, however, are rarely observed; asymmetric structures, such as "canes," are more common.[10] Experiments by Adrian *et al.*[10] in the subsonic regime have shown evidence of the streamwise clustering of multiple hairpin vortices into "packets." Hairpin packets have a mean angle of about 12°, and the induced velocity from the multiple hairpins creates a zone of retarded, streamwise velocity within the packet itself.[10] The hairpin packet model offers explanations for the bursting event and the streamwise persistence of the low-speed streaks at the wall. Evidence for hairpin packets in supersonic flows is lacking, as are data on packet properties, such as length, convection velocity, and internal hairpin spacing.

Direct numerical simulations by Martín[11] make available a detailed database of turbulent boundary layers over a range of freestream Mach numbers. We utilize this database to characterize the properties of the inner and outer boundary layer structure.

II. DNS parameters and accuracy

To investigate the variation of turbulent boundary layer structure with Mach number (M), we utilize an in-house DNS database that Martín[11] describes in detail. The freestream conditions for the calculations are atmospheric at 20 km altitude, and the Reynolds numbers for the mean flow profiles are the maximum values for which we can gather DNS statistics in a reasonable turnaround time. The number of grid points necessary for accurate DNS is determined by the ratio of the large to small scales, namely, $\delta^+ = \delta/z_\tau$, where z_τ is the near-wall length-scale and δ is the boundary layer thickness. For the present simulations δ^+ is kept at roughly 360, leading to an increase in the Reynolds number based on momentum thickness, Re_θ, with Mach number. The Reynolds number dependence in the near-wall region is eliminated when the data are plotted in wall units.

The boundary-layer-edge conditions for the DNS, as well as Re_θ, δ, and pertinent integral parameters, are given in table 1. The freestream Mach numbers for the database range from 3 to 5. For all computations the wall condition is isothermal, and we prescribe the wall temperature to be nearly the adiabatic temperature. Table 2 provides the grid resolution and domain size for the simulations. The streamwise, spanwise, and

Case	δ^+	L_x/δ	L_y/δ	L_z/δ	Δx^+	Δy^+	N_x	N_y	N_z
M3	325	9.1	2.3	13.8	8.0	3.0	384	256	106
M4	368	7.9	2.0	15.4	7.6	2.8	384	256	110
M5	382	7.4	1.8	14.0	7.4	2.8	384	256	110

Table 2. Grid resolution and domain size for the DNS.

wall normal directions are taken as x, y, and z, respectively.

The details of the numerical method and the evaluation of the DNS data are provided by Martín.[11] Here, we summarize the accuracy of the simulations. Figure 1(a) plots the van Driest transformed velocity profiles for the DNS data, showing good agreement between the prediction and the simulations. The skin friction coefficients given by the DNS as compared to the van-Driest II prediction are given in figure 1(b). The DNS skin friction lies within 8% of the prediction, denoted by the error bars.

III. Structure characterization methods

A. Average structure angle

We calculate the average structure angle in the (x, z)-plane as a function of wall-normal distance using two-point spatial correlations of the streamwise fluctuating mass-flux, $(\rho u)'$. The present method is similar to that employed in hotwire probe experiments, which instead use two-point space-time correlations, so that the DNS results can be compared directly with experimental data. The wall-normal distance between the correlated points, or "probe" separation, z_p, is fixed at some percentage of δ. We consider a given grid location (x_{ref}, z_{ref}) as the lower, fixed reference point, and vary the streamwise distance of the second point (at $z = z_{ref} + z_p$) from $x = x_{ref} - \delta$ to $x = x_{ref} + \delta$ to obtain a correlation profile. If a structure spanning both wall-normal locations is present and oriented at some angle to the wall, there will be a streamwise shift, x_p, in the correlation peak. The structure angle at each z-location is then computed as $\theta = \arctan(z_p/x_p)$; the wall-normal distance reported is the midpoint of the probe locations.

For each DNS time realization the structure angle is calculated in two streamwise, wall-normal planes separated by a spanwise distance of 0.75δ, so that the evaluated structures do not coincide. Spatial averaging is performed in the streamwise direction for each plane, and the results are ensemble-averaged over multiple time realizations having independent structures.

The computational grid in the wall-normal direction is stretched, so that obtaining flow parameters at desired wall-normal locations requires interpolation. Here we use linear interpolation.

The fixed wall-normal probe separation acts like a low-pass filter, so that the angle computation provides a sense of the average structure height at a given z-location. Larger probe separation therefore results in lower resolution. Figure 2 gives the average structure angle at Mach 3 using five different probe separations ranging from $z_p = 0.01\delta$ to 0.1δ. Correlation distances of 0.05δ or less give reasonable results very near the wall, but angles computed using $z_p = 0.01\delta$ and 0.025δ become unreliable above $z/\delta > 0.1$ and $z/\delta > 0.5$, respectively. Above the log layer ($z/\delta \approx 0.4$), where the structures are larger, the structure angle computation is essentially independent of probe separation for $z_p \geq 0.05\delta$; the hotwire data show a similar collapse as the probe separation is increased.[7] We present angle computations for $z_p = 0.05\delta$, which gives the best results over the largest range of z-values for all Mach numbers.

Figure 3 shows the average structure angle versus distance from the wall for the Mach 3 case. For comparison we plot results from the Mach 3, $Re_\theta = 81,000$ hotwire experiments of Spina *et al.*[7] and those of Bookey *et al.*[12] obtained from filtered Rayleigh scattering at conditions matching those of the DNS. Spina *et al.*[7] employed the two-point correlation method with $0.09\delta \leq z_p \leq 0.4\delta$ and reported angles ranging from 45° to 60° throughout most of the boundary layer; for clarity we plot only their measurements for $z_p = 0.09\delta$. We find reasonable agreement with the results of both experiments.

B. Integral scales

We investigate the variation in structure size with Mach number by calculating the integral scales, including their distributions, in the three grid directions. The longitudinal, transverse, and wall-normal integral scales are denoted as Λ_x, Λ_y, and Λ_z, respectively. They are computed from the conditional averages for $(\rho u_i(x_i))'(\rho u_i(x_i+\delta x_i))' > 0$, where we use the notation $(\rho u_i(x_i))'$ to represent the fluctuating quantity of the mass flux in the i-th direction as a function of x_i, as follows:

$$\Lambda_i = \left\langle \overline{\int_0^{Lx_i/2} (\rho u_i(x_i))'(\rho u_i(x_i+\delta x_i))' dx_i} / \overline{(\rho u_i(x_i))'^2} \right\rangle,$$

the over-bar and angle brackets denote spatial- and ensemble-averaging, respectively.

The longitudinal and transverse integral scales are determined in (x, y)-planes as a function of distance from the wall, with spatial averaging in the y- and x-directions, respectively. We compute Λ_z similar to the structure angle in two (x, z)-planes separated by 0.75δ for each time realization, with spatial averaging in the streamwise direction. This gives a single value for Λ_z, but further information on the wall-normal scales is provided by its probability density function (p.d.f.). The p.d.f. for each integral scale is estimated by binning the values at each grid location for each time realization, and normalizing using the number of samples.

We analyze the near-wall streaky structures by calculating the distributions of both Λ_x and the spanwise, low-speed streak spacing, λ_s. The low-speed streak locations are identified by considering only regions where the fluctuating velocity, u', is lower than a threshold. Changing the threshold by ±20% results in a less than 4% change in $\overline{\lambda_s}$, and similar λ_s distributions. Figure 4 shows p.d.f.'s of Λ_x and λ_s at $z^+ = 5$ and 15 for the Mach 3 case; the velocity thresholds used to determine λ_s at each location are $-0.05\overline{u(z)}$ and $-0.10\overline{u(z)}$, respectively. Plotted against the p.d.f.'s of λ_s are the incompressible results of Smith & Metzler,[5] who measured the spanwise spacing of the low-speed streaks for a turbulent boundary layer in a water channel at a similar Re_θ of 2030.

Figures 4(a–b) show that the average streamwise extent of the wall streaks for Mach 3 is about 1.6δ, with the distribution skewed toward values slightly smaller than the mean. The mean value of λ_s is $O(100)$ wall units, consistent with previous measurements at subsonic conditions (see figures 4c–d).[5] We find that the λ_s distributions at Mach 3 are similar to those for the incompressible case. However, the Mach 3 p.d.f.'s are more skewed toward lower values and exhibit somewhat narrower peaks. Additionally, the average streak spacing is less for Mach 3: at $z^+ = 5$, $\overline{\lambda_s^+} = 87$, compared to 93 for the water channel; at $z^+ = 15$, $\overline{\lambda_s^+}$ is 95 for Mach 3 and 114 for the incompressible experiments. The increase in average streak spacing with distance from the wall for Mach 3 is in agreement with the experimental data at incompressible conditions.[5]

C. Vortex convection velocity

We determine the convection velocity of the vortex structures observed in the streamwise, wall-normal planes by first identifying them using a threshold of the swirling strength, λ_{ci}, and then conditionally averaging their streamwise velocities. Adrian *et al.*[10] utilized a similar technique to measure the convection velocity of hairpin vortex heads (transverse vortices) in an incompressible turbulent boundary layer at $Re_\theta = 7705$, using velocity data in streamwise, wall-normal planes from digital particle image velocimetry. The swirling strength distinguishes between the rotating flow of compact vortices and regions dominated by shear.[13]

Adrian *et al.*[10] identified hairpin heads using the criteria that λ_{ci} should be a local maximum and above a threshold, then conditionally averaged the streamwise velocity at these locations. A conservative threshold, $\lambda_{ci,\, threshold} > 30\overline{\lambda}_{ci}$, was chosen to ensure that the velocity data averaged corresponded to compact vortices.

We use the same $\lambda_{ci,\, threshold}$, and consider only points that both lie outside the buffer region and have vorticity of the same sign as that of a hairpin head, i.e., positive. These criteria occasionally identify tall regions of λ_{ci} that correspond to the "leg" of a hairpin vortex, which may include a head vortex above it. We utilize a scheme devised as part of our hairpin packet-finding algorithm to determine if an identified structure is a leg, or other large vortical structure, that exceeds a predetermined maximum vortex head size ($0.1\delta \times 0.1\delta$). If this is the case, the scheme checks if a head vortex exists at the structure's upper extreme. If so, we discard the remaining structure; if not, we discard the entire structure (see section VI for details). For each DNS time realization we identify vortices in two streamwise, wall-normal planes separated by a spanwise distance of 0.75δ (so that the structures in each plane are independent), and then average the streamwise velocities of the identified regions. Next the results are ensemble-averaged over multiple time realizations having independent structures.

Figure 5 shows the resulting vortex convection velocity versus distance from the wall, superimposed on the mean streamwise velocity, for the Mach 3 case; the incompressible data from Adrian *et al.*[10] are included for comparison. We find that the vortex convection velocity lags that of the mean flow for $z/\delta < 0.6$. Adrian *et al.*[10] reported the same trend for $z/\delta > 0.4$, but found that the vortex and mean velocities are coincident closer to the wall. The scatter in the vortex convection velocity above $z/\delta = 0.5$ for both studies is due to the relatively small number of vortices identified in this region by the threshold of λ_{ci}.

IV. Structure variation with Mach number

A. Average structure angle

Figure 6 shows the average structure angle for the three DNS cases. We find that, in general, the structure angle increases with Mach number. For Mach 4, the angle is essentially greater than that of Mach 3 for $0.15 < z/\delta < 0.55$, with overlap elsewhere; for $z/\delta > 0.9$ the Mach 4 angle is actually smaller. The Mach 5 structure angle is significantly larger than that of the other two cases throughout the boundary layer, which is most likely due to compressibility effects (see below). For the subsonic case, at $M = 0.1$ and $Re_\theta = 5000$, Alving *et al.*[14] measured structure angles ranging from 25° to 45°, somewhat lower than those found for the Mach 3 DNS and the measurements of Spina *et al.*[7] The moderate Reynolds number angle data of Alving *et al.*[14] and the current DNS support the conclusion that increasing the Mach number results in larger average structure angles.

B. Integral scales

Figure 7 plots the longitudinal and spanwise integral scales, Λ_x and Λ_y, respectively, versus distance from the wall. The structure size is $O(\delta)$ in the streamwise direction and between 90 and 110 wall units in the spanwise direction. Both the streamwise and spanwise integral scales reach a local maximum in the viscous sublayer, with the exception of the Mach 5 spanwise scale. At Mach numbers 3 and 4, the spanwise integral scale grows with distance from the wall in the log region. For Mach 5, Λ_y exhibits a slight minimum at $z^+ = 7$ and remains relatively constant for $z^+ > 20$.

We observe a significant decrease in the streamwise extent of the structures with increasing Mach number, and a small decrease in the spanwise structure length. Smits & Dussauge[15] compared data at subsonic conditions to the Mach 3 results of Spina *et al.*[7] and found similar trends: the streamwise length scales at Mach 3 were two to three times smaller than those of the incompressible flows, while the spanwise length scale was nearly independent of the Mach number. The smaller streamwise scale at higher Mach numbers reflects the corresponding increase in the average structure angle.

The p.d.f.'s of Λ_x and Λ_y for Mach 3–5 are given in figures 8 and 9, respectively, which plot results

Case	$\overline{\lambda_s^+}(5)$	$\sigma_{\lambda_s}(5)$	$\overline{\lambda_s^+}(15)$	$\sigma_{\lambda_s}(15)$	$M(5)$	$M'(5)$	$M(15)$	$M'(15)$
M0[5]	95	40	114	48	-	-	-	-
M3	87	43	95	53	0.48	0.18	1.13	0.33
M4	84	43	92	52	0.52	0.21	1.27	0.39
M5	75	34	87	42	0.60	0.24	1.43	0.45

Table 3. Statistics on spanwise streak spacing for Mach 3–5 and incompressible flow,[5] as a function of wall-normal distance in wall units.

at three wall-normal locations in the inner layer: one in the viscous sublayer ($z^+ = 15$) and two in the logarithmic region ($z^+ = 40$, $z^+ = 70$); Λ_x is also plotted in the wake region at $z/\delta = 0.6$. Figure 8(b) shows the significant decrease in Λ_x near the wall with higher Mach number, and also that the skewness toward smaller values increases with Mach number. The distribution of the streamwise length scale at all Mach numbers widens with distance from the wall in the log layer, and the skew of the Mach 4 and 5 data increases. Although the Mach 3 and 4 distributions become narrower in the outer region, the Mach 5 p.d.f. continues to broaden.This behavior at Mach 5, along with the significant skew toward smaller values, may be due to compressibility effects, discussed below.

Figure 9 shows that the distribution of the spanwise length scale does not change significantly with Mach number or distance from the wall in the inner layer. In the upper logarithmic region, at $z^+ = 70$, the p.d.f. becomes broader toward larger values for Mach 3 and 4, while the Mach 5 p.d.f. is nearly unchanged. These trends account for the behavior of the average Λ_y given in figure 7.

The wall-normal integral scale, Λ_z, is 0.28δ, 0.29δ, and 0.36δ for Mach numbers 3, 4, and 5, respectively, so that it increases with Mach number. However, because the wall-normal direction contains multiple length scales, it is more informative to examine how the p.d.f. of Λ_z varies with Mach number (see figure 10). As expected, at all Mach numbers the p.d.f.'s show two peaks corresponding to the inner and outer length scales. We observe that the peak due to smaller structures occurs at nearly the same value for all three Mach numbers, $\Lambda_z/\delta \approx 0.09$, which is the height of the viscous sublayer. However, the peak-location (Λ_z/δ) corresponding to the large-scale structures increases from Mach 3–5. Therefore, the large-scale structures become taller with increasing Mach number. This is consistent with the average structure angle data, which indicate that the structures are more upright at higher Mach numbers.

Figure 11 gives the distribution of λ_s at $z^+ = 5$ and 15 for Mach 3–5, including the incompressible results of Smith & Metzler[5] for $Re_\theta = 2030$. The supersonic p.d.f.'s possess somewhat narrower peaks, and are skewed toward slightly lower values. Both the incompressible and supersonic distributions broaden toward larger values with greater distance from the wall, which Smith & Metzler[5] attributed to an increase in streak merging and intermittency. Table 3 gives the mean and standard deviation, σ_{λ_s}, of the streak spacing for Mach 3–5 and the incompressible case at both $z^+ = 5$ and 15; included for reference are the mean and fluctuating number, $M(z)$ and $M'(z)$, respectively (the latter is defined in section V). The mean Mach number at $z^+ = 5$ is less than 1 for all three DNS cases, and greater than 1 at $z^+ = 15$. Table 3 shows that the average streak spacing decreases with local Mach number at both wall-normal locations, and is relatively lower at $z^+ = 5$ than $z^+ = 15$. Additionally, σ_{λ_s} increases slightly from the incompressible case to Mach 3, but decreases with local Mach number to below the incompressible value at Mach 5. We therefore find the general trend that the streak spacing becomes narrower and more uniform with increasing Mach number.

C. Vortex convection velocity

The streamwise vortex convection velocity for Mach 3–5, obtained in (x, z)-planes as described in section IIIC, is plotted in figure 12. For $z/\delta \leq 0.4$ the vortex convection velocity is less than the mean velocity at all Mach numbers. Above this location, the vortex velocity data overlap with the mean velocity; there is greater scatter in the vortex convection velocity in the outer flow because the criteria identify fewer vortices there. In the log layer ($0.1 \leq z/\delta \leq 0.4$) we find that the vortex convection velocity, normalized by U_∞, increases with increasing Mach number. As with the average structure angle, the difference in convection velocity from Mach 4 to 5 is more substantial than from Mach 3 to 4.

V. Compressibility effects

The substantial change in the average structure properties from Mach 4 to 5 may be due to the onset of compressibility effects. A measure of compressibility is the fluctuating Mach number, M', which is the local variation in the Mach number from the mean. It is usually assumed that compressibility effects become important when M' reaches 0.3. We compute M' as

$$M' = \left\langle \frac{u}{a} \right\rangle - \frac{\langle u \rangle}{\langle a \rangle},$$

and find that it attains values over 0.5 for Mach 5, while the peak values for Mach 3 and 4 are .42 and 0.44, respectively (see figure 13). For Mach 5, the instantaneous M' reaches maximum values slightly greater than 1, unlike the Mach 3 and 4 cases, so that the occurrence of shocklets is more likely. Using the shock detection algorithm of Taylor & Martín[16] extended to boundary layers, we identify any shocklets and their strength in the DNS data. Figure 14 shows the average shocklet strength for each Mach number versus distance from the wall. We find that the Mach 5 DNS exhibits the highest density of shocklets, and that the Mach 5 shocklets are stronger. The shocklets are found primarily below $z/\delta = 0.2$ and in the outer layer, consistent with the plot of M'. Shocklets may act to impede or "chop" coherent vortical structures, possibly causing the higher structure angles and shorter streamwise integral scales calculated for Mach 5. Figure 15 shows vortical structures identified in DNS volumes at Mach 3 and 5 using a single contour of the discriminant of the velocity gradient tensor. Similar to λ_{ci}, the discriminant highlights regions of spiraling flow, consistent with that of compact vortices, when it attains values greater than zero.[17] We find that the Mach 5 case does not exhibit the longer, continuous structures found at Mach 3, which is consistent with an increased presence of shocklets. These shocklet effects may also lead to broader or skewed length scale distributions, as observed for the Mach 5 p.d.f.'s of Λ_x.

VI. Hairpin vortex packets in DNS data

A review of the DNS data in streamwise, wall-normal planes revealed "signatures" of hairpin vortex packets as described by Adrian *et al.*[10] We find from visual inspection that hairpin packets are a relatively common phenomenon, with at least a few signatures present in each (x, z)-plane. The packet-finding algorithm described below identified an average of three to ten hairpin packets per independent (x, z)-plane for Mach numbers 3–5, respectively, each consisting of two to three vortices.

Figure 16 shows contours of vorticity in a single (x, z)-plane at Mach 3, with velocity vectors and a single contour of λ_{ci}. A constant speed of $0.75U_\infty$ has been subtracted from the streamwise velocity vector to highlight the rotational flow of vortices in that convective frame. A group of three vortices, identified by λ_{ci} and lying between $x/\delta = 3.75$ and 4.5, exhibit the characteristics of a hairpin packet signature: they form a shallow downstream angle with the wall, their streamwise spacing is relatively small, and there is a region of low streamwise velocity below them. Additionally, the vortices in the packet travel at about the same streamwise velocity, as the velocity vectors show rotational flow for each vortex in the frame chosen. To determine if these three vortices represent the heads of hairpins in a packet, we plot the three-dimensional

Case	Angle (°)	Height ($^+$)	Height (δ)	Length (δ)	U_{packet}/U_∞	Spacing (δ)	Heads
M3	24.6	94	0.31	0.34	0.69	0.14	2
M4	19.4	87	0.28	0.43	0.70	0.15	3
M5	16.9	86	0.22	0.43	0.73	0.15	3

Table 4. Hairpin packet properties for Mach 3–5.

flow structure in figure 17 using the same value of λ_{ci} to generate an iso-surface; the (x, z)-plane from figure 16 is included in the volume for reference. We find that the vortices observed in the (x, z)-plane at $y/\delta = 0$ are the result of hairpin-like structures, i.e. head- and cane-like vortices, impinging that plane from both the positive and negative y-directions.

After establishing the existence of hairpin packets, we devised a scheme to identify packets and characterize their properties, namely, angle, length-scale, convection velocity, height, and the spacing between hairpins. The algorithm first finds hairpin head vortices in the (x, z)-plane using the criteria that λ_{ci} must be greater than $10\overline{\lambda ci}$ and that the out-of-plane vorticity is larger than three standard deviations from the mean; only the region outside the buffer layer is considered. These criteria occasionally identify hairpin legs, or tall vortical structures, that may or may not be attached below a hairpin head in the plane under consideration. The algorithm uses a maximum head-vortex size criterion, $0.1\delta \times 0.1\delta$, and flags identified structures that are larger than this as legs. It then checks for a head above the leg by testing whether the location of maximum λ_{ci} is within 0.1δ (the head height) from the top of the leg. If a head is found, only the head region is kept. If no head is found, the structure is discarded.

Next, the location of the core of each vortex is determined by assuming that the core coincides with the maximum of λ_{ci} for that vortex. For each (x, z)-plane considered, the algorithm chooses the vortex that is closest to the location $(x = 0, z = z_{buffer})$ as the reference vortex for the first packet. It then searches for the next downstream vortex that is both within a downstream distance of 0.05δ and at an angle α from the reference vortex, such that $0 < \alpha < 45°$ (with respect to the wall). If a vortex satisfying these criteria is found, it is considered to be part of a hairpin packet with the reference vortex, and is taken as the new reference vortex. The process continues until no new vortices belonging to the first packet are found. New packets are searched for in the same manner, until all identified vortices in the x-z plane are accounted for.

It is worth mentioning that the hairpin packet-finding algorithm searches only for groups of hairpin heads that conform to the ideal case described by the hairpin packet model.[10] Adrian *et al.*[10] point out that some packets exhibit a negative downstream angle, and that not every vortical structure is part of a packet. Additionally, recent evidence from both compressible and incompressible studies suggests that multiple hairpin packets may align in the spanwise direction and stack together lengthwise to form what are termed "very large scale motions" (VLSM), with streamwise lengths greater than 20δ.[18,19] These structures are not captured within the domain length of the current DNS. <This issue is discussed further in section VII.>

Once any hairpin packets are identified, finding the packet properties is straightforward. We determine the packet angle by calculating the arctangent of the slope of the least-squares-fit through the packet vortex cores; the packet height is taken as the z-location of the highest vortex core in the packet. The packet convection velocity is computed as the average streamwise velocity of the data points comprising each vortex in the packet. We generate statistics on the average packet properties for each Mach number by considering data in two streamwise, wall-normal planes for each DNS time realization, and ensemble-averaging the results over multiple time realizations with independent structures, in the same manner as the structure angle calculation described in section IIIA.

Location	$L_x = 9.1\delta$	$L_x = 24\delta$
$z^+ = 5$	24.6%	23.1%
$z^+ = 15$	37.0%	35.7%
$z/\delta = 0.2$	36.8%	38.8%

Table 5. Percentage of energy contained in the low-speed streaks at different wall-normal locations for domains of length 9.1δ and 24δ.

Table 4 gives the average hairpin packet properties for each Mach number. We find that the average packet angle decreases from 24.6° at Mach 3 to 16.9° at Mach 5. These values are above the average angle of 12° found by Adrian *et al.*[10] for their incompressible boundary layer at $Re_\theta = 7705$, but within the range that they observed. Further simulations with matching Re_θ and varying Mach number are needed to better isolate the effect of Mach number.

We observe that the average spacing between hairpins within a packet does not vary significantly with Mach number, and is about 0.15δ or 54 wall units. This is less than half of the spacing observed by Adrian *et al.*[10] Packet length increases from 0.34δ at Mach 3 to 0.43δ at Mach 4 and 5, due primarily to the increase in the average number of hairpin heads. Adrian *et al.*[10] reported an average packet length of 1.3δ, or three times that reported here, for their $Re_\theta = 7705$ case, which follows from the larger hairpin spacing of the incompressible case. We find that both the streamwise integral scale and average packet length decrease by about a factor of three from the incompressible to the supersonic case.

Table 4 shows that the average packet height decreases moderately with increasing Mach number, while the convection velocity becomes slightly larger, ranging from 0.31δ (94 wall units) to 0.22δ (86 wall units) and $0.69U_\infty$ to $0.73U_\infty$, respectively, for Mach 3–5. Adrian *et al.*[10] measured packets of comparable height, and found packets reaching at most 0.8δ, as well as similar convection velocities. We find an average of 2 vortex "heads" per packet at Mach 3, increasing to 3 for Mach 4 and 5. This falls within the range observed by Adrian *et al.*,[10] who reported 2–3 hairpin heads per packet for their low Reynolds number case ($Re_\theta = 930$), which increased to over 10 at higher Re_θ.

The average hairpin packet properties provide an overall picture of the packet variation with Mach number. As the Mach number increases, the hairpin vortex packets are closer to the wall and faster, and lean more toward the wall. This is contrary to the Mach number variation of the average coherent structure height and angle, but consistent with the vortex convection velocity trend reported above. Individual structures may be less resilient to local, small-scale transient shocks (shocklets) than larger, organized packets, which could explain the observed discrepancy. We find that although the spacing between hairpin heads within a packet does not change significantly with Mach number, the average packet length increases from Mach 3 to Mach 4 because the number of heads increases by one.

Figure 18 shows examples of hairpin packets found by the above algorithm for Mach numbers 3, 4, and 5. The figures show streamwise, wall-normal planes with contours of vorticity, as well as "boxes" marking the identified hairpin heads in the packet and velocity vectors relative to the packet convection velocity. We find that the hairpin packets identified by the algorithm typically exhibit low-velocity zones below them, consistent with the packet model and experiments at incompressible conditions.[10,19]

VII. Very large scale motions

Previous studies have shown that the alternating streaks of positive and negative velocity fluctuation found in the inner layer carry a significant portion of the turbulence energy.[19,20] Experiments provide evidence that these streaky structures have streamwise lengths exceeding 20δ, which is significantly larger than the 9.1δ domain length of the Mach 3 DNS.[18,19] We determine the energy contribution of the low-speed streaks to the total turbulence energy at three wall-normal locations for the Mach 3 case. To test whether the streak energy contribution changes with domain length, L_x, we performed a DNS at Mach 3 with $L_x = 24\delta$.

We compute the streamwise turbulence energy by first calculating the two-dimensional spectra of the streamwise velocity in the (x, y) plane under consideration using a two-dimensional Fourier transform. The spectra is then integrated over the domain to obtain the energy. To determine the energy contribution from the low-speed streaks, we isolate them using a velocity threshold (as was done to find the streak spacing in sec IIIB), such that only points where u' is less than the threshold are considered. We then compute the spectra over the entire plane with the velocity at grid points not associated with streaks set to zero. We consider two wall-normal locations in the viscous sublayer, $z^+ = 5$ and 15, and one in the log region at $z/\delta = 0.2$. The velocity thresholds at each height are $-0.05\overline{u(z)}$, $-0.10\overline{u(z)}$, and $-0.05\overline{u(z)}$, respectively.

Table 5 gives the streak energy as a percentage of the total at each wall-normal location for $L_x = 9.1\delta$ and $L_x = 24\delta$. We find that the energy content does not change significantly with L_x. The low-speed streaks contain about 24% of the streamwise turbulence energy very near the wall at $z^+ = 5$, and over one-third of the energy in the buffer region ($z^+ = 15$) and in the log layer at $z/\delta = 0.2$.

The effect of increasing the computational domain length on Λ_x is illustrated in figure 19. We observe that increasing L_x by a factor of 2.6 results in a similar increase in Λ_x.

VIII. Conclusions

We develop methods for analyzing the structure of supersonic turbulent boundary layers at Mach numbers from 3 to 5 using a DNS database. The results are in good agreement with the available experimental data. We find significant variation in the average structure properties with Mach number. Both the structure angle and convection velocity increase with increasing Mach number, while the streamwise structure extent decreases. The change in the various structure properties is self-consistent. For example, the structure height increases as the structure angle becomes larger. Compressibility effects may be responsible for the significant change in the structure properties at Mach 5. For Mach 5 we find maximum fluctuating Mach numbers greater than 1 and an increased number of shocklets, which may act to impede or "chop" the coherent vortical structures. The spanwise spacing of the low-speed streaks at the wall is observed to decrease slightly and become more regular with increasing Mach number, as compared to the experimental data at incompressible conditions. Analysis of the DNS data reveals hairpin vortices arranged in closely spaced streamwise packets, similar to what has been observed in incompressible flows. We develop a scheme to search for and characterize these hairpin packets, and calculate the variation in the average packet properties with Mach number. We find that the hairpin packets convect faster, grow longer, and contain more hairpin heads with increasing Mach number. Conversely, the packet angle and height exhibit the opposite behavior, while the hairpin spacing remain essentially constant.

We compute the energy of the low-speed streaky structures as compared to the overall turbulence, and find that the streaks in the buffer and log layers carry slightly over one-third of the total energy. Although increasing the computational domain length increases the streamwise integral scale by a similar factor, we find no significant variation in the energy of the low-speed streaks with domain length.

Acknowledgments

We would like to acknowledge the support from the Air Force Office of Scientific Research under grant no. AF/F49620-02-1-0361.

References

[1]Klebanoff, P., "Characteristics of turbulence in a boundary layer with zero pressure gradient," Tech. rep., NACA Report 1247, 1955.

[2]Runstadler, P., Kline, S., and Reynolds, W., "An experimental investigation of flow structure of the turbulent boundary layer," Tech. rep., Mechanical Engineering Department, Stanford University Report MD-8, 1963.

[3]Kline, S., Reynolds, W., Schraub, F., and Runstadler, P., "The structure of turbulent boundary layers," *Journal of Fluid Mechanics*, Vol. 30, 1967, pp. 741–773.

[4]Bakewell, Jr., H. and Lumley, J., "Viscous sublayer and adjacent wall region in turbulent pipe flow," *Physics of Fluids*, Vol. 10, 1967.

[5]Smith, D. and Metzler, S., "The characteristics of low-speed streaks in the near-wall region of a turbulent boundary layer," *Journal of Fluid Mechanics*, Vol. 129, 1983, pp. 27–54.

[6]Kim, H., Kline, S., and Reynolds, W., "The production of turbulence near a smooth wall in a turbulent boundary layer," *Journal of Fluid Mechanics*, Vol. 50, 1971, pp. 133–160.

[7]Spina, E., Donovan, J., and Smits, A., "On the structure of high-Reynolds number supersonic turbulent boundary layers," *Journal of Fluid Mechanics*, Vol. 222, 1991, pp. 293–327.

[8]Head, M. and Bandyopadhyay, P., "New aspects of turbulent boundary-layer structure," *Journal of Fluid Mechanics*, Vol. 107, 1981, pp. 297–338.

[9]Kline, S. and Portela, L., "A view of the structure of turbulent boundary layers," *Self-sustaining mechanisms of wall turbulence. Advances in fluid mechanics series.*, edited by R. Panton, Vol. 15, Computational Mechanics Publications, Southhampton, UK and Boston, USA, 1997, pp. 167–180.

[10]Adrian, R., Meinhart, C., and Tomkins, C., "Vortex organization in the outer region of the turbulent boundary layer," *Journal of Fluid Mechanics*, Vol. 422, 2000, pp. 1–54.

[11]Martín, M. P., "DNS of hypersonic turbulent boundary layers," *AIAA Paper No. 2004-2337*, 2004.

[12]Bookey, P., Wyckham, C., and Smits, A., "Experimental investigations of Mach 3 shock-wave turbulent boundary layer interactions," *AIAA Paper No. 2005-4899*, 2005.

[13]Zhou, J., Adrian, R., Balachandar, S., and Kendall, T., "Mechanisms for generating coherent packets of hairpin vortices in channel flow," *Journal of Fluid Mechanics*, Vol. 387, 1999, pp. 353–396.

[14]Alving, A., Smits, A., and Watmuff, J., "Turbulent boundary layer relaxation from from complex curvature," *Journal of Fluid Mechanics*, Vol. 211, 1990, pp. 529–556.

[15]Smits, A. J. and Dussauge, J.-P., *Turbulent shear layers in supersonic flow*, Springer, 2nd ed., 2006.

[16]Taylor, E. M. and Martín, M. P., "Stencil adaptation properties of a WENO scheme in direct numerical simulations of compressible turbulence," *to appear in Journal of Scientific Computing*, 2006.

[17]Chong, M. S., Perry, A. E., and Cantwell, B. J., "A general classification of three-dimensional flow fields," *Physics of Fluids A*, Vol. 2, No. 5, 1999, pp. 765–777.

[18]Ganapathisubramani, B., Clemens, N., and Dolling, D., "Large-scale motions in a supersonic turbulent boundary layers," *Journal of Fluid Mechanics*, Vol. 000, 2006, pp. 1–11.

[19]Hutchins, N. and Marusic, I., "Investigation of the log region structure in wall bounded turbulence," Paper 2006-325, American Institute of Aeronautics and Astronautics, 2006.

[20]Ganapathisubramani, B., Longmire, E. K., and Marusic, I., "Characteristics of vortex packets in turbulent boundary layers," *Journal of Fluid Mechanics*, Vol. 478, 2003, pp. 35–46.

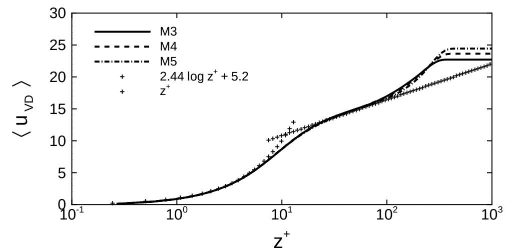

(a)

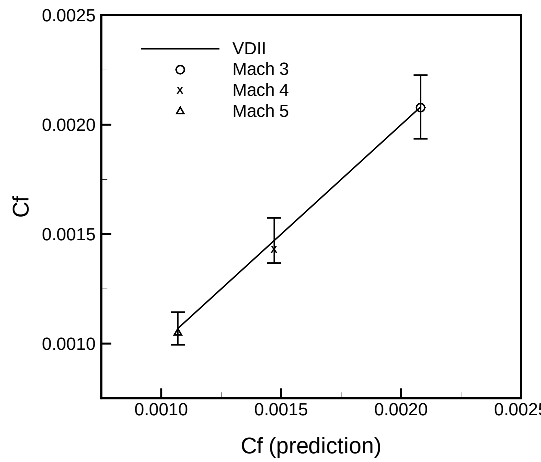

(b)

Figure 1. (a) Mean velocity profiles and (b) skin friction coefficients for the DNS.

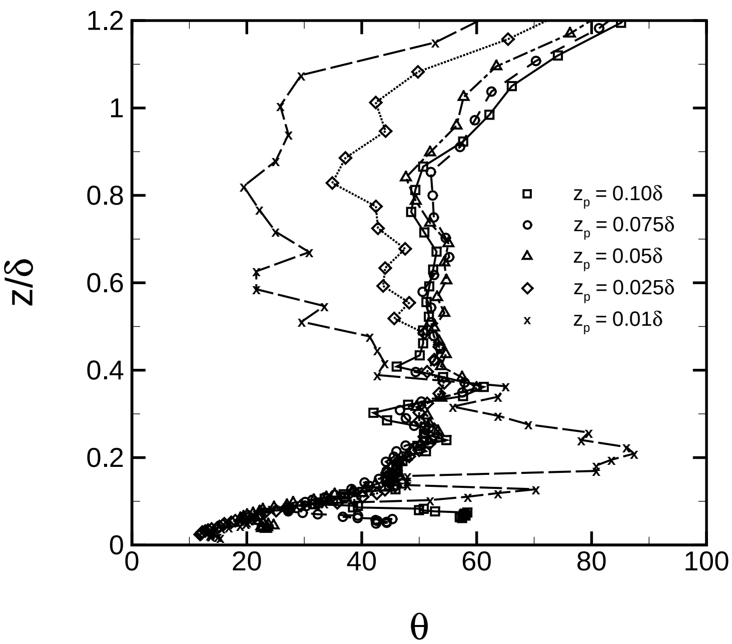

Figure 2. Average structure angle for Mach 3, computed using five different wall-normal probe separations, z_p.

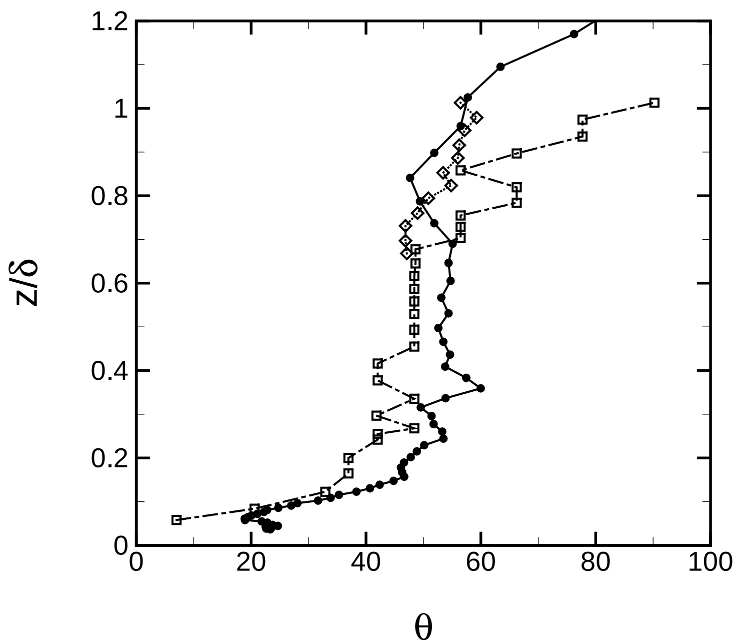

Figure 3. Average structure angle in the (x, z)-plane, $M = 3$. •——, DNS, using 2-point correlations of $(\rho u)'$ with $z_p = 0.05\delta$, $Re_\theta = 2390$; □–.–, hotwire measurements from Spina *et al.*,[7] 2-point correlations of $(\rho u)'$ with $z_p = 0.09\delta$, $Re_\theta = 81000$; ◊....., measurements from Bookey *et al.*[12] using filtered Rayleigh scattering, $Re_\theta = 2400$.

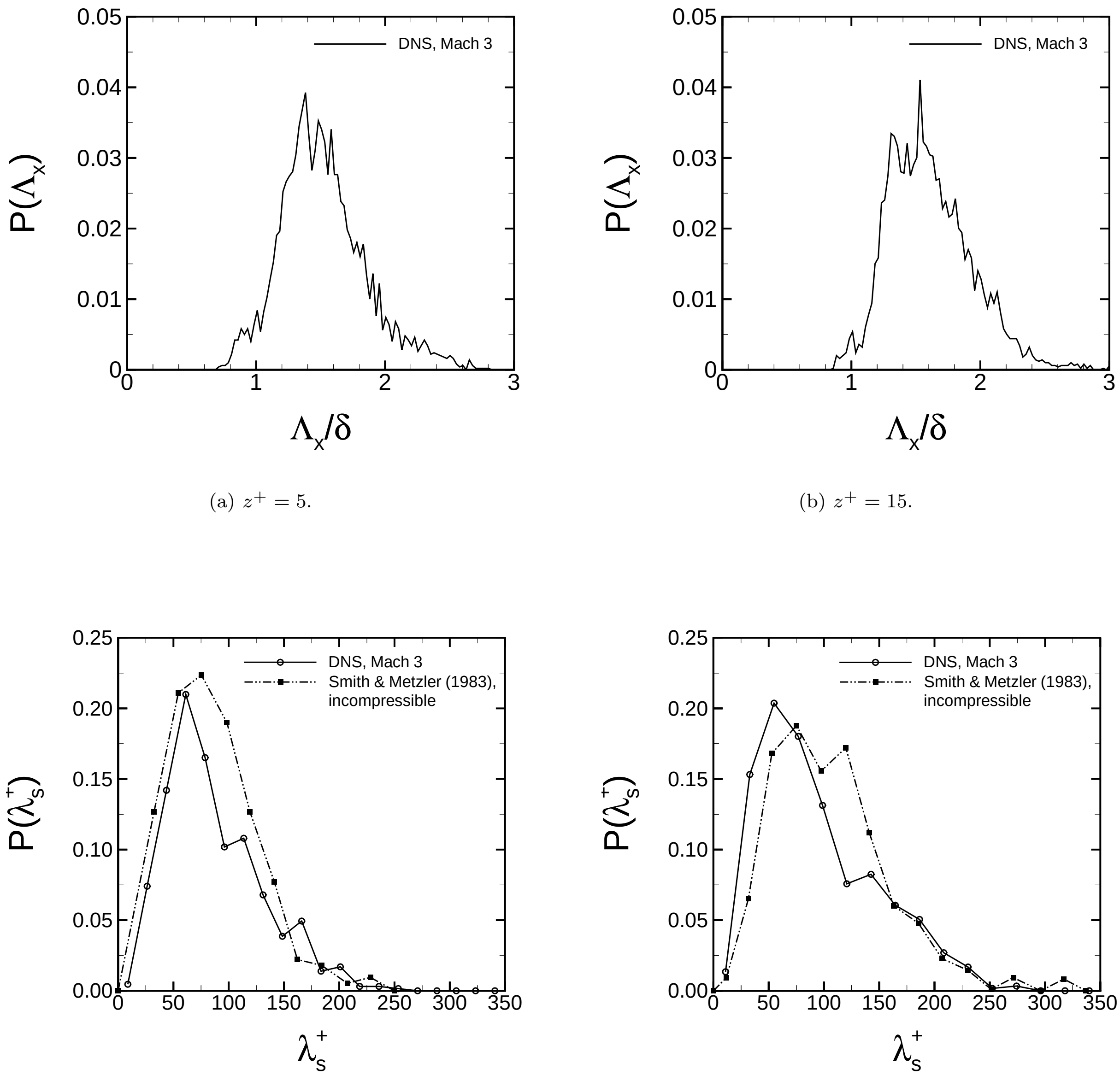

(a) $z^+ = 5$.

(b) $z^+ = 15$.

(c) $z^+ = 5$.

(d) $z^+ = 15$.

Figure 4. Probability-density functions of the longitudinal integral length scales, Λ_x, and the spanwise low-speed streak spacing, λ_s, in the viscous sublayer at Mach 3. The incompressible λ_s data of Smith & Metzler[5] are plotted for comparison.

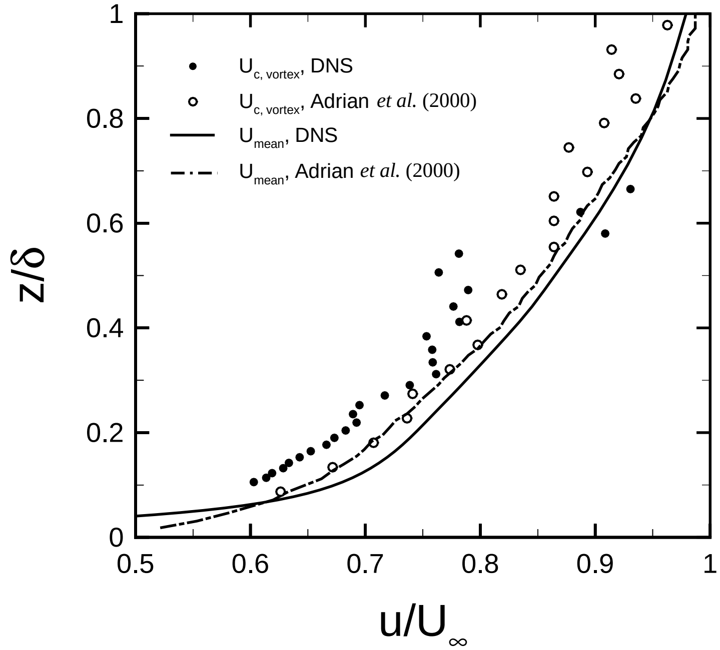

Figure 5. Vortex streamwise convection velocity superimposed on the mean velocity profile. DNS conditions: $M = 3$, $\boldsymbol{Re_\theta} = 2390$; **Adrian *et al.*:**[10] **incompressible,** $\boldsymbol{Re_\theta} = 7705$.

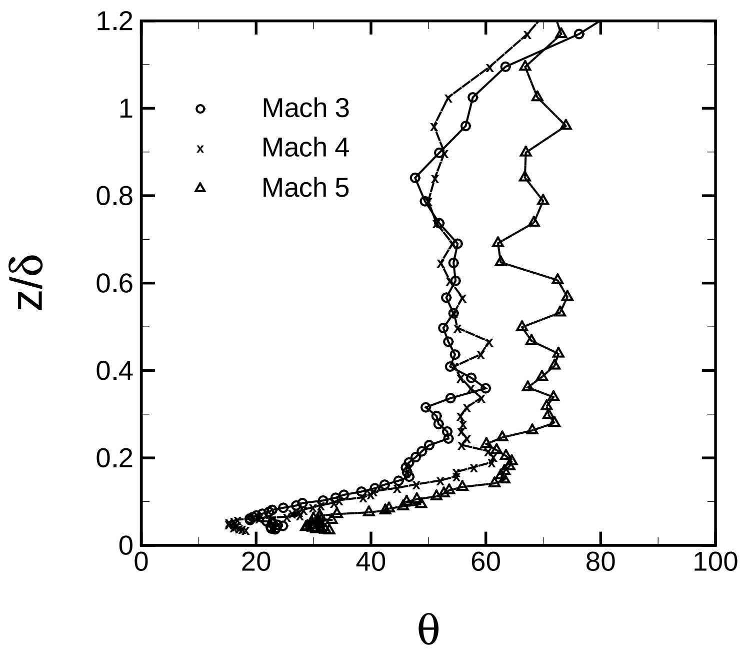

Figure 6. Average structure angle vs. Mach number in the (x, z)**-plane using 2-point correlations of** $(\rho u)'$ **with** $z_p = 0.05\delta$.

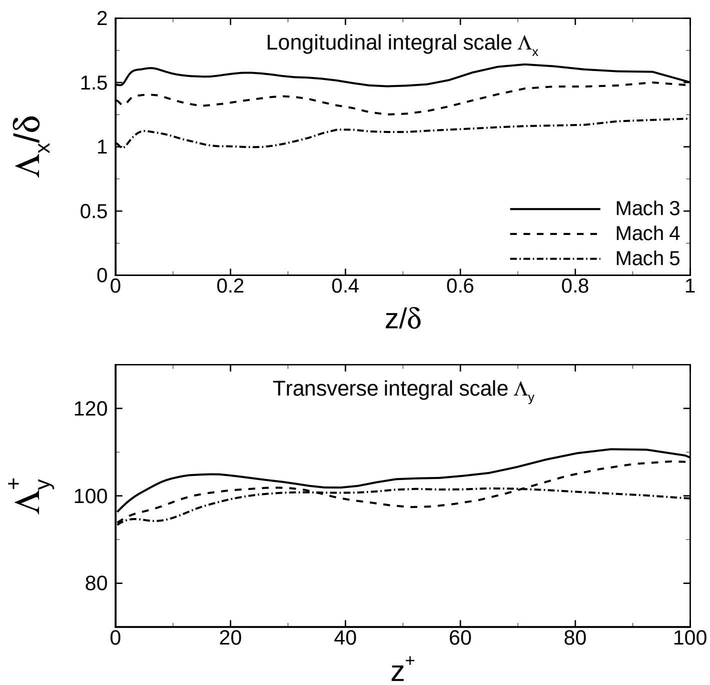

Figure 7. Longitudinal and transverse integral length scales, Λ_x and Λ_y, respectively, vs. Mach number.

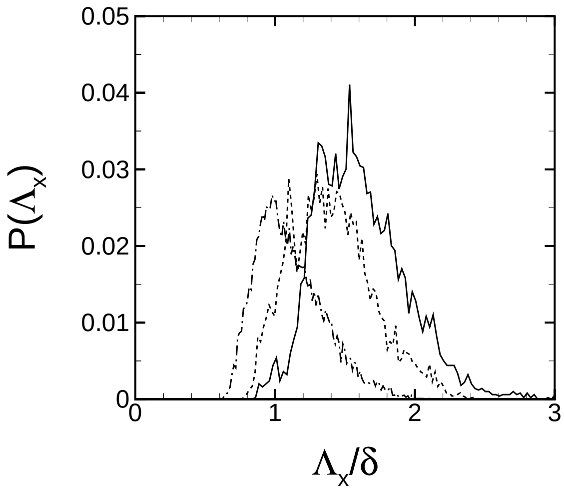

(a) $z^+ = 15$.

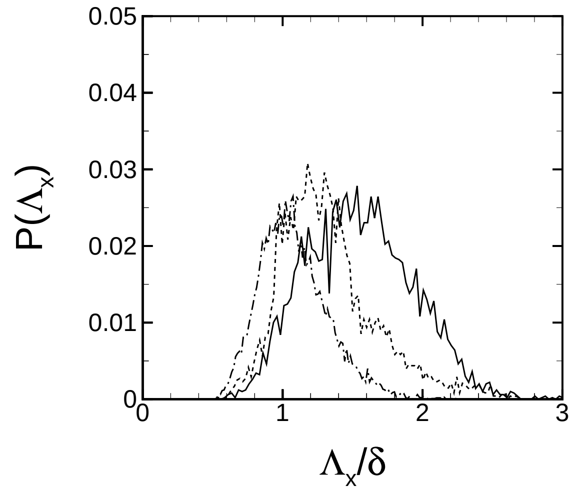

(b) $z^+ = 40$.

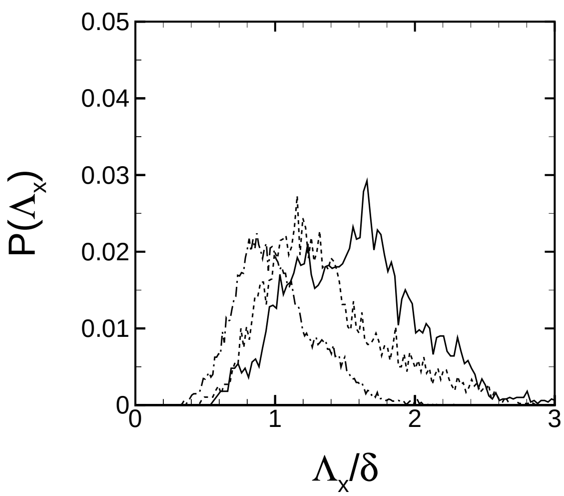

(c) $z^+ = 70$.

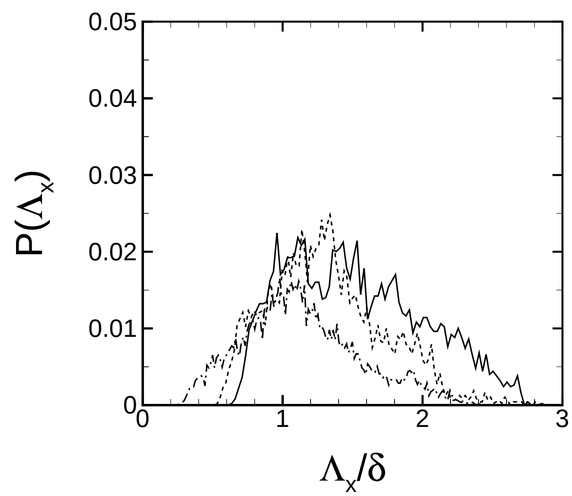

(d) z/δ=0.6.

Figure 8. Probability-density functions of the longitudinal integral length scale, Λ_x, in the viscous sublayer, log layer, and wake region vs. M. ——, Mach 3; – –, Mach 4; –.–, Mach 5.

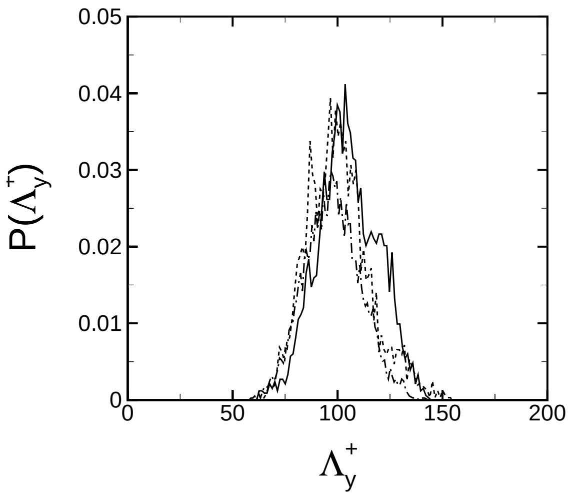

(a) $z^+ = 15$.

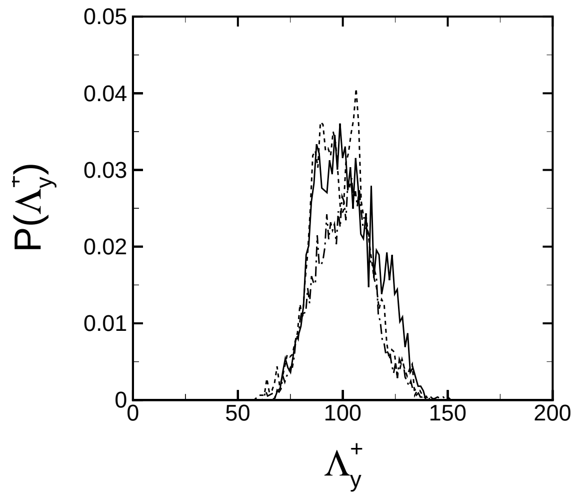

(b) $z^+ = 40$.

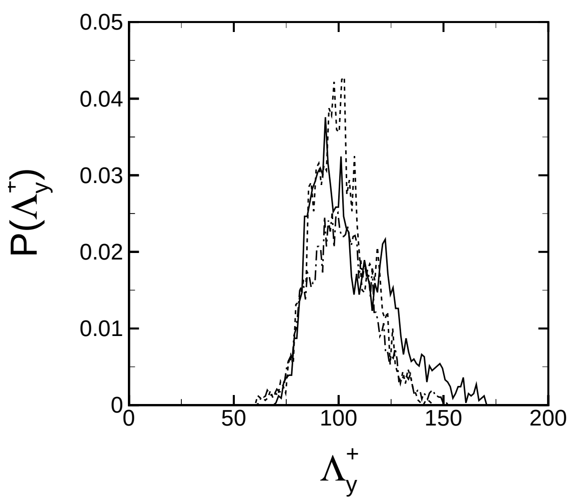

(c) $z^+ = 70$.

Figure 9. Probability-density functions of the transverse integral length scale, Λ_y, in the viscous sublayer and the log region vs. M. ——, Mach 3; – –, Mach 4; –.–, Mach 5.

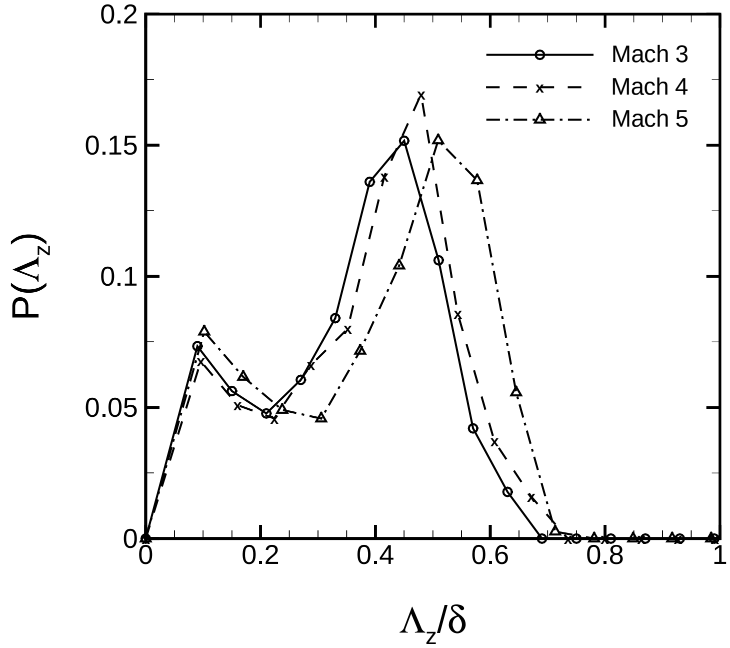

Figure 10. Probability-density function of the wall-normal integral length scale, Λ_z, vs. M. ○——, Mach 3; ×– –, Mach 4; △–.–, Mach 5.

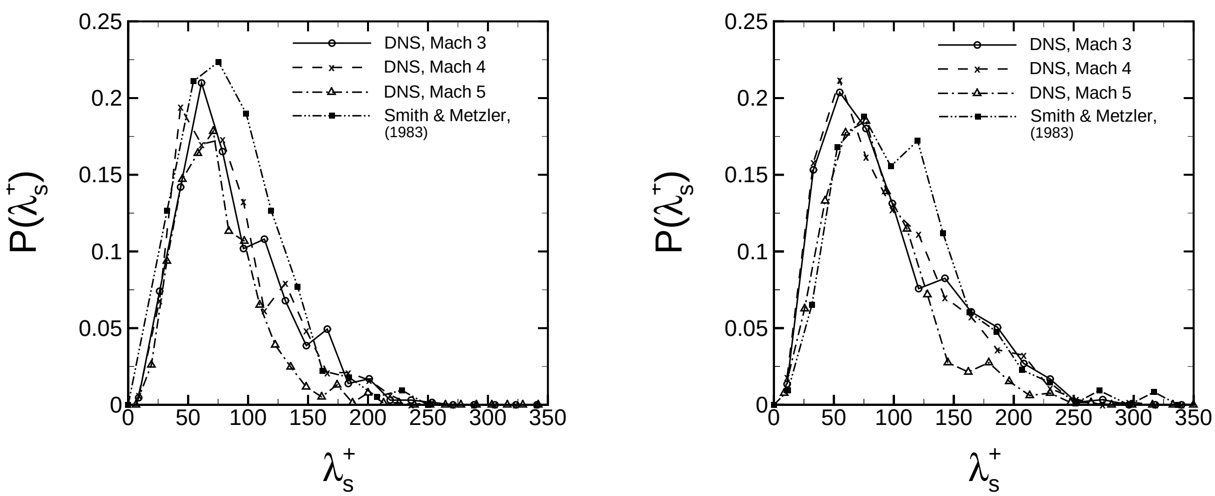

(a) $z^+ = 5$.

(b) $z^+ = 15$.

Figure 11. Probability-density functions of the spanwise streak spacing, λ_s, in the viscous sublayer vs. Mach number.

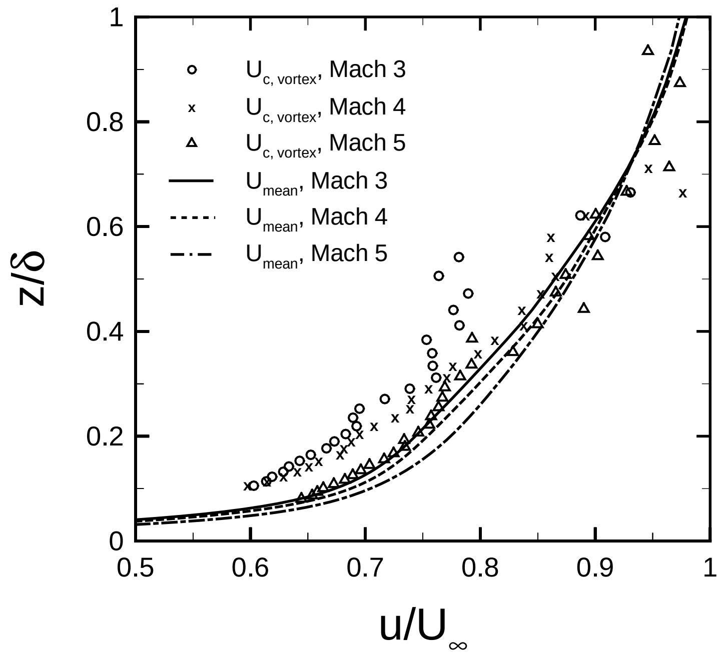

Figure 12. Vortex streamwise convection velocity vs. Mach number, superimposed on the mean velocity profiles.

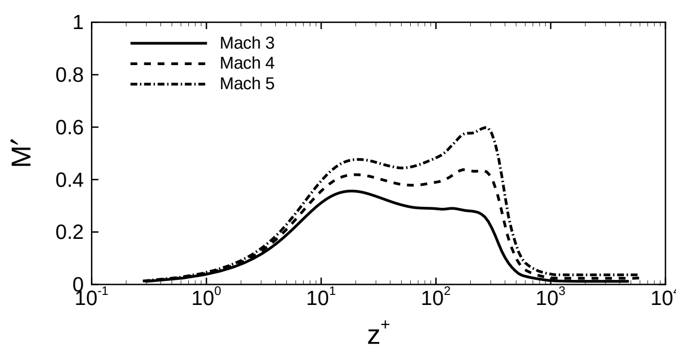

Figure 13. Fluctuating Mach number, M'.

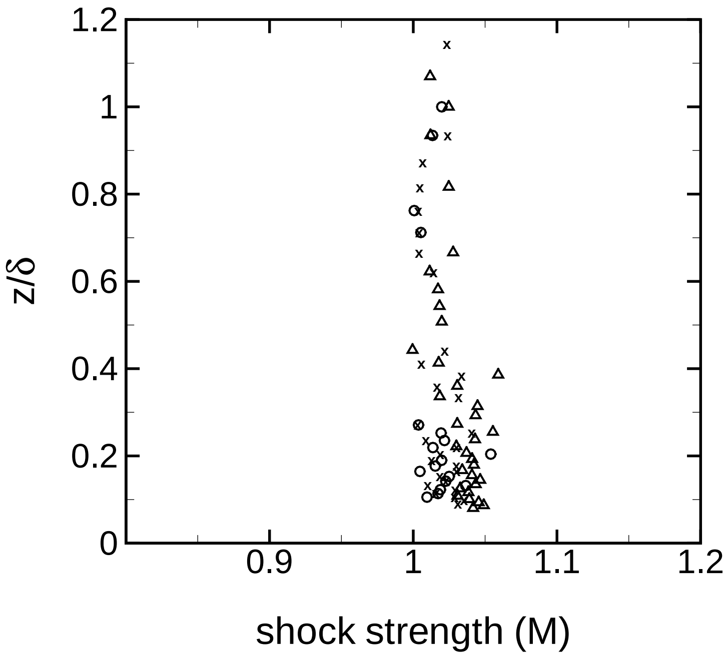

Figure 14. Shocklet strength vs. Mach number. ○——, Mach 3; ×– –, Mach 4; △–.–, Mach 5.

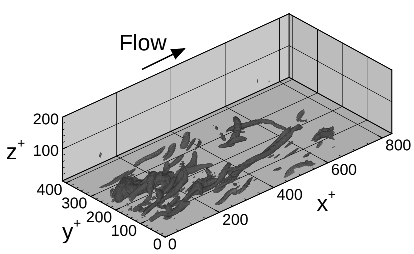

(a) Mach 3

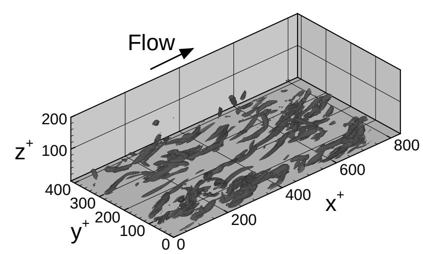

(b) Mach 5

Figure 15. Structures identified using an iso-surface (10^{-4} of maximum value) of the discriminant of the velocity gradient tensor at Mach 3 and 5.

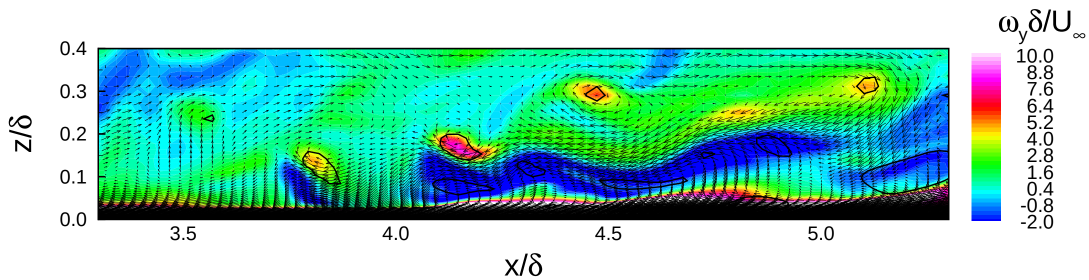

Figure 16. Example of a hairpin packet from the DNS data (see text for description). $M = 3$, $\boldsymbol{Re}_\theta = 2390$.

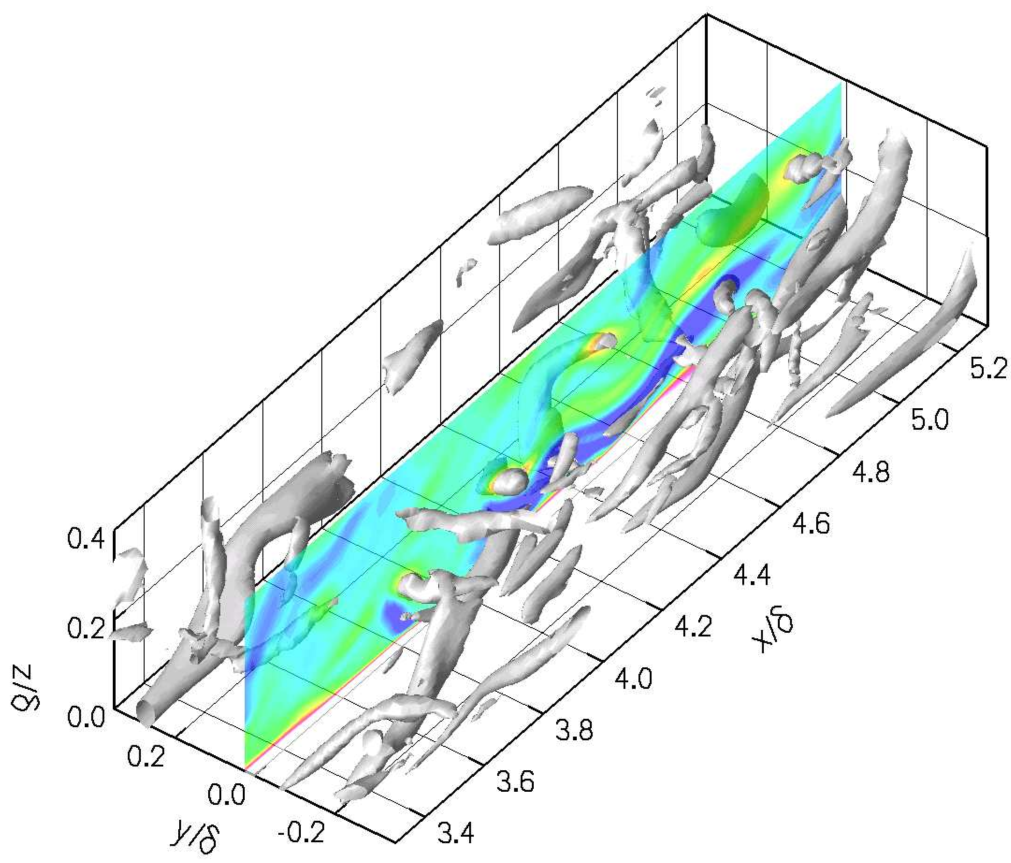

Figure 17. Evidence of hairpin structures arranged in a packet. The structures are visualized using an iso-surface of λ_{ci}**. The** (x, z)**-plane data of Figure 5 are included for reference, with colored contours showing spanwise vorticity.** $M = 3$, $\boldsymbol{Re}_\theta = 2390$.

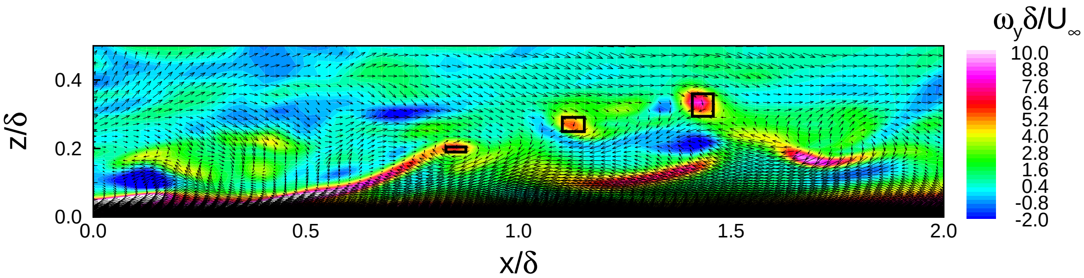

(a) Mach 3.

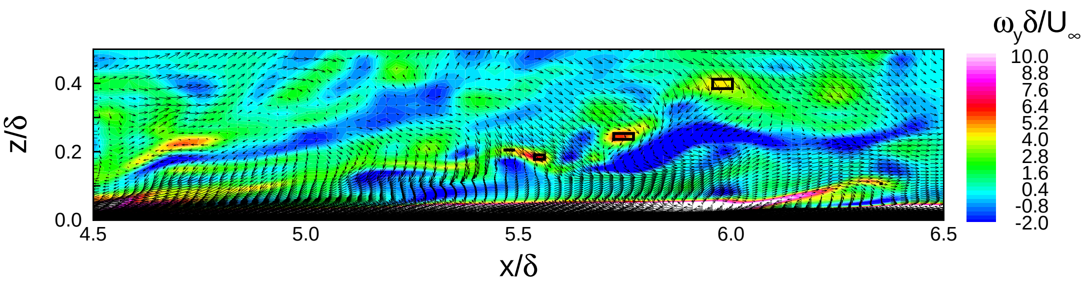

(b) Mach 4.

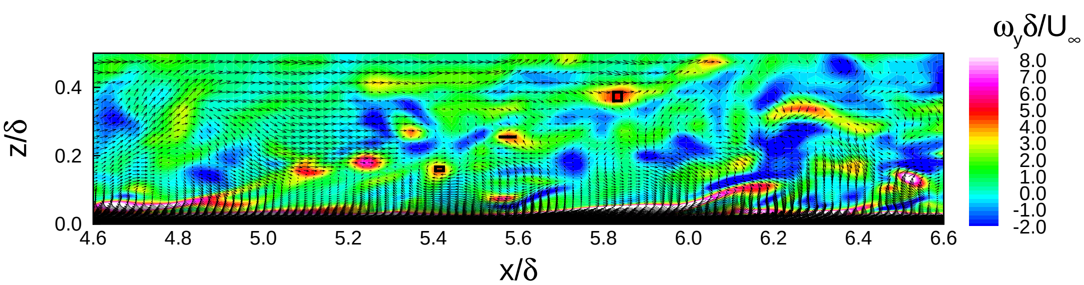

(c) Mach 5.

Figure 18. Examples of hairpin packets found by the algorithm at Mach 3, 4, and 5. The black boxes mark the hairpin heads identified by the algorithm to be part of a packet. Constant speeds of $0.67U_\infty$, $0.70U_\infty$, and $0.72U_\infty$ have been subtracted from the streamwise velocity vector for Mach 3, 4, and 5, respectively, to highlight the rotational flow of vortices in the convective frame of the packet.

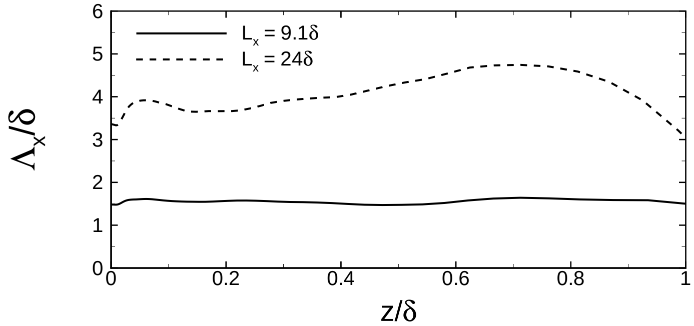

Figure 19. Longitudinal integral length scale, Λ_x, for streamwise computational domains lengths of 9.1δ and 24δ at Mach 3.